

# Non-equilibrium solidification behavior associated with powder characteristics during electron beam additive manufacturing



Yufan Zhao<sup>a</sup>, Huakang Bian<sup>b,\*</sup>, Hao Wang<sup>b</sup>, Aoyagi Kenta<sup>b</sup>, Yamanaka Kenta<sup>b</sup>, Akihiko Chiba<sup>b,\*</sup>

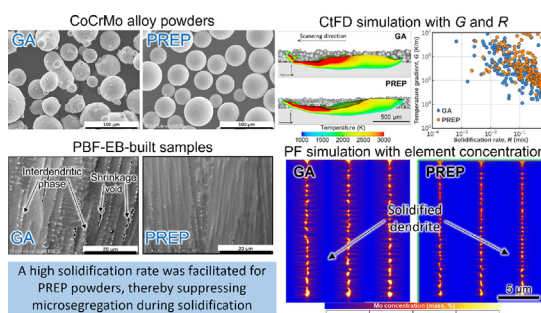
<sup>a</sup> State Key Laboratory of Solidification Processing, Northwestern Polytechnical University, Xi'an, Shaanxi 710072, PR China

<sup>b</sup> Institute for Materials Research, Tohoku University, 2-1-1 Katahira, Aoba-ku, Sendai, Miyagi 980-8577, Japan

## HIGHLIGHTS

- The mechanism that powder features influence non-equilibrium solidification was revealed.
- The formation of  $\sigma$  phase and shrinkage void in interdendritic region was suppressed in PREP sample.
- High solidification rate obtained by melting on PREP powder layer contributed to the microsegregation suppression.
- The effect of molten pool morphology on solidification rate was determined by the thermal properties of powder layer.

## GRAPHICAL ABSTRACT



## ARTICLE INFO

### Article history:

Received 23 March 2022

Revised 22 June 2022

Accepted 30 June 2022

Available online 2 July 2022

### Keywords:

Powder bed fusion with electron beam

CoCrMo alloy

Heat flow and solidification

Microsegregation

Multi-scale simulations

## ABSTRACT

For components built by powder bed fusion with electron beam (PBF-EB), the resulting microstructure arising from non-equilibrium solidification, microsegregation and the formation of interdendritic phases significantly affects the material properties. Notably, the powder characteristics influence the heat absorption and conduction, thereby altering the molten pool behavior and solidification parameters. However, the effect of the powder feedstock on solidification during PBF has not been widely investigated. In this study, a CoCrMo alloy was fabricated using powders prepared by gas-atomization (GA) and plasma rotating electrode process (PREP). Under the given operating conditions, samples built using the two powders were characterized and compared. By performing multi-scale numerical simulations, melting and solidification were visualized and analyzed to elucidate the mechanism through which the powder characteristics influence the non-equilibrium solidification behavior during PBF-EB. The study revealed that after appropriate size control, compared with the GA powder, the PREP powder had a smaller specific surface area and higher sphericity; thus, the generated powder layer exhibited higher heat absorption and dissipation rates. Therefore, a high solidification rate was facilitated, thereby suppressing microsegregation. These findings contribute to PBF knowledge related to feedstock, proving to be an essential reference for selecting and optimizing metallic powders applicable to additive manufacturing.

© 2022 The Authors. Published by Elsevier Ltd. This is an open access article under the CC BY-NC-ND license (<http://creativecommons.org/licenses/by-nc-nd/4.0/>).

\* Corresponding authors.

E-mail addresses: [huakang.bian.d5@tohoku.ac.jp](mailto:huakang.bian.d5@tohoku.ac.jp) (H. Bian), [akihiko.chiba.d3@tohoku.ac.jp](mailto:akihiko.chiba.d3@tohoku.ac.jp) (A. Chiba).

## 1. Introduction

A controlled microstructure is a vital prerequisite for improving the suitability and stability of additively manufactured

components [1]. Powder bed fusion (PBF) can be categorized into two methods based on the heat source: PBF with laser (PBF-L) and PBF with electron beam (PBF-EB) [2]. In addition to the material composition [3,4], the PBF processing conditions, including the machine parameters [5,6], environmental status [7,8], heat treatment [9], and feedstock characteristics [10,11], synthetically govern the final solidification microstructure and performance.

During PBF, rapid and non-equilibrium solidification occurs in a highly transient manner, and a translating molten pool forms within the powder layer, producing unusual microstructure of multi-component alloys [12]. In addition to the size and morphology of the solidified grains, the substructures resulting from microsegregation and associated interdendritic phase significantly influence the mechanical properties [13] and hot cracking resistance [14]. The enrichment of solute elements in the interdendritic melt alters the local thermodynamics and promotes second-phase formation [15]. The matrix and interdendritic phases react differently to force and deformation, thereby deteriorating their mechanical properties. Moreover, the formation of a long-chain-shaped interdendritic phase with a low melting point results in liquation cracking [16]. Therefore, research has focused on controlling non-equilibrium solidification in MAM-built components.

Previous studies have shown that element partitioning and the degree of microsegregation depend on the solidification parameters [17]. Particularly, the solidification rate (i.e., solid-liquid interface velocity) is crucial for determining the degree of microsegregation. Solute trapping occurs when the solidification rate is higher than the partial element diffusion rate at the solidification front, because of incomplete element partitioning [18]. Nie et al. [19] studied the relationship between molten pool thermal conditions and Nb microsegregation during the solidification of a direct energy deposition (DED)-built Inconel 718 alloy. They found that a low-temperature gradient with a high cooling rate (i.e., a high solidification rate) decreases the Laves phase fraction. Similarly, simulation studies conducted by Kumara et al. [20] and Wang et al. [21] determined the number of reduced Laves phases with an increased cooling rate, which was generated by a low-power input. Xiao et al. [22] compared two laser modes of DED and found that, compared to the continuous-wave laser, the quasi-continuous-wave laser suppressed Nb segregation and Laves phase formation because of the increased solidification rate. Wang et al. [23] evaluated the effect of the laser scan speed on microsegregation in a PBF-built Fe-C alloy and concluded that a high scan speed accompanied by a high solidification rate resulted in a low interdendritic segregation ratio because of solute trapping. Moreover, Chen et al. [24] and Zhang et al. [25] performed an additional substrate cooling process using water and liquid nitrogen to promote rapid solidification and suppress microsegregation.

To date, to achieve microsegregation control, most existing studies, including those mentioned above, have focused on altering the solidification rate by manipulating the power, scan speed, and environmental conditions (e.g., substrate cooling). Notably, in PBF, powder characteristics, such as particle size distribution, morphology, and surface features, influence heat transfer, thereby altering the molten pool behavior and solidification conditions [26]. A previous study showed that the amounts of interdendritic phases and shrinkage voids were significantly different in samples built using two Inconel 718 alloy powders (gas-atomization (GA) and the plasma rotating electrode process (PREP)) [27]. Under a given operating condition, the utilization of powders with different characteristics affects solidification. However, most studies have primarily evaluated the effect of the bulk properties of the powder layer (e.g., packing density and layer thickness) on the quality of the formed alloy [28], whereas few studies have been conducted to explore the mechanism through which the powder characteris-

tics influence the non-equilibrium solidification behavior during PBF-EB.

CoCrMo (CCM) alloys are widely used in bone implants. Considering the advantages of PBF, custom-shaped implants are considered more favourable [29]. Elucidating the relationship between the solidified microstructure and powder characteristics will provide a novel theoretical basis for defect suppression and flexible microstructure control. Therefore, in this study, following our previous study [27] using Inconel 718 alloy powder, the effect of the CCM alloy powder characteristics on the non-equilibrium solidification behavior in PBF-EB was examined. PBF-EB of the CCM alloy was performed using two CCM alloy powders prepared by GA and PREP. The two powders exhibited different particle size distributions (PSDs) and particle morphologies. Under a given building condition, samples built with two different powders were characterized, and the solidification microstructure and compression properties were compared. During PBF-EB, EB interacts with the powder layer to form a high-speed moving molten pool, accompanied by rapid solidification [30]. It is difficult to acquire solidification parameters, microstructure evolution, and spatial solute distribution using the experimental method from this highly transient and localized process [31]. Therefore, a multi-scale numerical simulation framework was developed. The framework consists of simulations accounting for powder spreading, molten pool formation, and solidification based on the discrete element method (DEM), computational thermal-fluid dynamics (CtFD), and phase field (PF). Melting and solidification were visualized and analyzed to demonstrate the mechanism through which powder characteristics influence non-equilibrium solidification during PBF-EB. The findings of this study contribute to PBF knowledge related to feedstocks, proving to be an essential reference for selecting and optimizing metallic powders applicable to additive manufacturing.

## 2. Materials and methods

### 2.1. Materials and experiments

Two types of CCM powders prepared by GA (Sanyo Special Steel Co., Ltd., Himeji, Japan) and PREP (Fukuda Metal Foil & Powder Co., Ltd., Kyoto, Japan) methods were used for PBF-EB manufacturing. Fig. 1 shows the scanning electron microscopy (SEM) images, PSD, and circularity of the two powders. Many irregularly shaped particles were observed in the GA powder, resulting from the turbulent impact of high-speed gas flow on the molten metal during the GA process [32,33]. In contrast, most PREP powders exhibit a near-perfect spherical shape. PREP allows the formation of spherical powders through centrifugal granulation such that melt droplet translation follows a relatively stable trajectory and does not easily interfere with other droplets [34]. The high-sensitivity (HS) circularity of the two powders was evaluated using image analysis. In addition to the particle morphology, the two CCM powders showed differences in PSD, which was measured using a laser diffraction particle size analyzer. The chemical compositions of the two low-carbon (<0.15, mass%) CCM alloy powders (Table 1), which were examined using inductively coupled plasma atomic emission spectroscopy, showed subtle differences. The effect of this composition differences on solidification will be examined using phase-field simulation. By applying the average composition as the input, a phase diagram (Supplementary Material 1) illustrating the equilibrium phase fraction as a function of temperature was acquired using Thermo-Calc [35] and suggested that no carbides were present, whereas the  $\sigma$  phase may be embedded in the  $\gamma$ -FCC matrix after solidification.

Regarding PBF-EB manufacturing, the cuboid samples with an edge length of 10 mm were fabricated on a baseplate of SUS304

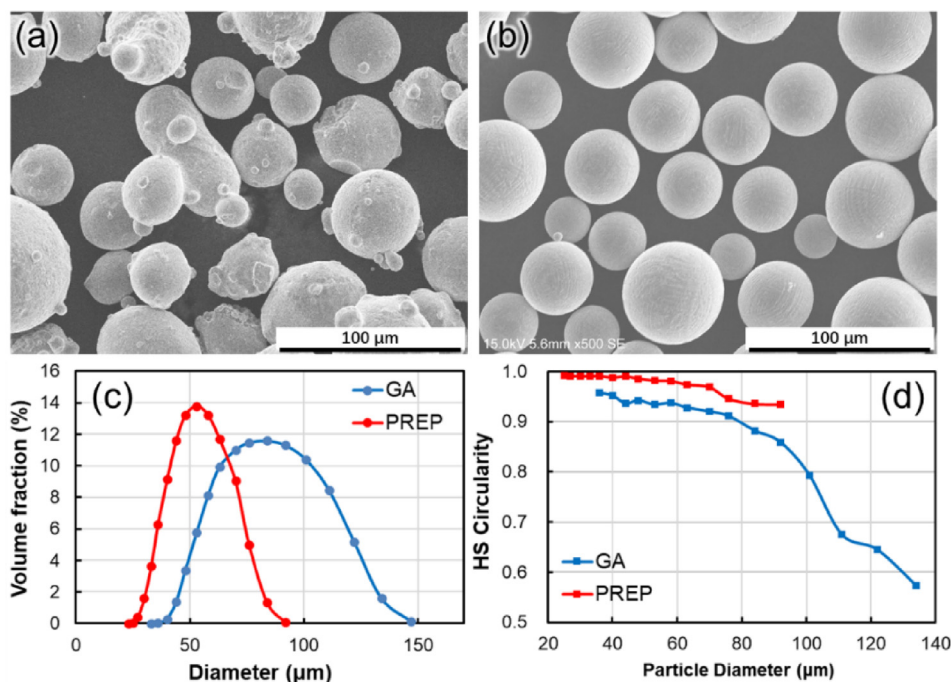


Fig. 1. SEM microscopy of the CCM powders fabricated by (a) GA and (b) PREP and their corresponding (c) PSD and (d) HS circularity.

Table 1

Chemical composition (mass%) of CCM alloy powders.

	Cr	Mo	Si	Mn	Fe	C	N	Ni	O	Co
GA	27.45	6.21	0.43	0.51	0.33	0.027	0.117	<0.05	0.0006	Bal.
PREP	27.30	5.71	0.39	0.45	0.09	0.048	0.078	<0.05	0.0014	Bal.

stainless steel using an Arcam® A2X machine (Arcam, GE Additive, Sweden). In the xy-scanning mode, the scanning direction was rotated by 90° per layer (Supplementary Material 2). The block samples were sectioned along the building direction using a wire electric discharge machine. After grinding and polishing, the solidified microstructure was observed by electron backscattered diffraction (EBSD) and SEM using a backscattered electron (BSE) detector. Focused ion-beam milling was conducted to prepare samples for scanning transmission electron microscopy (STEM) observations. The lattice structure and local elemental distribution were identified using STEM energy-dispersive X-ray (EDX) mapping. Compression tests were performed to evaluate the mechanical properties.

## 2.2. Multi-scale numerical simulation

A multi-scale numerical simulation framework was developed to simulate powder layer spreading, molten pool formation, and solidification based on DEM, CtFD, and PF, respectively (Supplementary Material 2). The simulations are described in Sections 2.2.1, 2.2.2, and 2.2.3.

### 2.2.1. DEM simulation for powder layer generation

A numerical model of the powder layer spreading was established using DEM to simulate the dynamic particle behaviour [36]. According to the governing force–displacement/rotation formulas, the particle–particle and particle–object interactions at the contact point are generated. The soft-contact mode allows for particle overlap, such that the contact force is calculated depending on the deformation [37]. In this study, a powder bed generation

analog was simulated using Yade, an open-source DEM framework [38]. Taking the PSD and powder mechanical properties as inputs, the three-dimensional arrangement data of the powder layer after spreading can be obtained [39]. A detailed description of the contact law (the nonlinear elastic Hertz–Mindlin no-slip contact model) and energy dissipation approach (viscous damping), which are suitable for the analysis of the actual metallic powder layer spreading during PBF, can be found in a recently published article [26]. The physical property-related parameters applied in the DEM simulation are listed in Supplementary Material 3. Notably, in the conventional DEM simulation, the powder particles were set to perfect spheres by default. A special particle clumping treatment was implemented to assemble the particles, by which irregular particles, such as elongated and satellite particles, could be constructed [27]. For the GA powder, the proportion of clumped particles was adjusted to match the experimental powder sphericity. Therefore, it is possible to evaluate particle morphology-related effects.

### 2.2.2. CtFD simulation for molten pool formation

An energy beam irradiates the powder layer to form a high-speed moving molten pool, which occurs through transient and localized heat and mass transfer processes [40]. To accurately acquire solidification information, including the molten pool geometry and solidification parameters, a numerical model for PBF-EB under specific environmental and operating conditions was established. A 3D numerical melting model was developed using FLOW-3D® [41]. The physical effects (i.e., buoyant flow, Marangoni convection, and vapor recoil pressure) that determine the fluid behavior and necessary heat transfer modes (i.e., conduction,

convection, and radiation) are included. An EB with a certain penetration depth was modelled as a volumetric heat source. Melting simulations of the two powders were performed using the DEM 3D powder layer data as the geometric configuration of the CtFD computational domain. The solidification parameters (i.e., the temperature gradient and solidification rate) of the evolutive solidification front were obtained. A description of the CtFD modeling with salient features for PBF-EB, the thermophysical properties of the CCM alloy, and parameters related to the simulation implementation are available in literature [42,43].

### 2.2.3. PF simulation for solidification with micro-segregation

The PF method is a powerful approach for the quantitative modeling of complex microstructural evolution kinetics [44]. Combined with the temperature and composition, the PF can simulate non-equilibrium processes. A 2D solidification model was established using a commercial PF software, MICRESS® [45] which was developed based on the multi-PF concept [46] and allows the management of multi-component alloys during various processes, such as solidified grain growth [47] and solid-state phase transformation [48]. The required thermodynamic data and atomic diffusion mobility that govern the microstructure evolution with solute diffusion can be obtained through direct coupling with the CALPHAD database via the interface with Thermo-Calc. For the CCM alloy, the PF simulation included Co, Cr, Mo, Mn, Si, and Fe. The 2D computational domain was placed in a 1D thermal field, where the temperature gradient originated from the bottom up, and was coupled with a constant cooling rate at the bottom. The initial  $\gamma$ -FCC nuclei, whose  $[0\ 0\ 1]$  preferred crystal growth orientation was parallel to the temperature gradient, were placed at the bottom of the computational domain. Coupled with the thermal field obtained from the CtFD simulation, the PF simulation allows the illustration of non-equilibrium solidification behavior with spatial solute distribution. The parameters used in the PF simulations are listed in Supplementary Material 4.

## 3. Results

### 3.1. Microstructure and compression property

The PBF-EB-built CCM cuboid samples were fabricated using GA and PREP powders. The processing parameters (power = 600 W, scan speed = 1000 mm/s, line offset = 200  $\mu\text{m}$ , preheating temperature = 1123 K, nominal layer thickness = 70  $\mu\text{m}$ ) were applied based on a previous study [49] to ensure excellent forming quality. Fig. 2 shows the grain morphology and crystallographic textures of the two samples. In both the GA and PREP samples, the columnar grain arrays are parallel to the building direction (BD, z-axis) with strong  $\langle 0\ 0\ 1 \rangle$  alignments along the z-axis and a  $\langle 0\ 0\ 1 \rangle$  fiber texture around the z-axis in the xy-plane, which is a result of the competitive growth of epitaxial grains within a typically directional temperature gradient [50,51]. Because most grains are columnar, in addition to the normal grain diameter, the grain size is characterized by the grain intercept length. The number of horizontal intercept lines was one-third of the number of EBSD scan rows. The results showed almost no difference between the as-built GA and PREP samples in terms of the grain morphology, grain size, and crystallographic texture.

Fig. 3 shows the BSE micrographs of the grain substructure in the two samples. Generally, the cellular dendrites grew parallel to the BD owing to the thermal flow direction and epitaxial growth feature during PBF-EB. By comparing the two samples, it was found that whether at the top or middle of the GA sample, the bright precipitates appeared at the interdendritic region, and some are long and chain-like. Notably, similar to the interdendritic phase, some striped voids are also arranged at the interdendritic region. These voids are thought to be caused by solidification shrinkage. The interdendritic shrinkage void is formed owing to the liquid feeding deficiency at the interdendritic region during solidification [52]. In contrast, in the PREP sample, the number of interdendritic phases was significantly reduced compared with that in the GA sample,

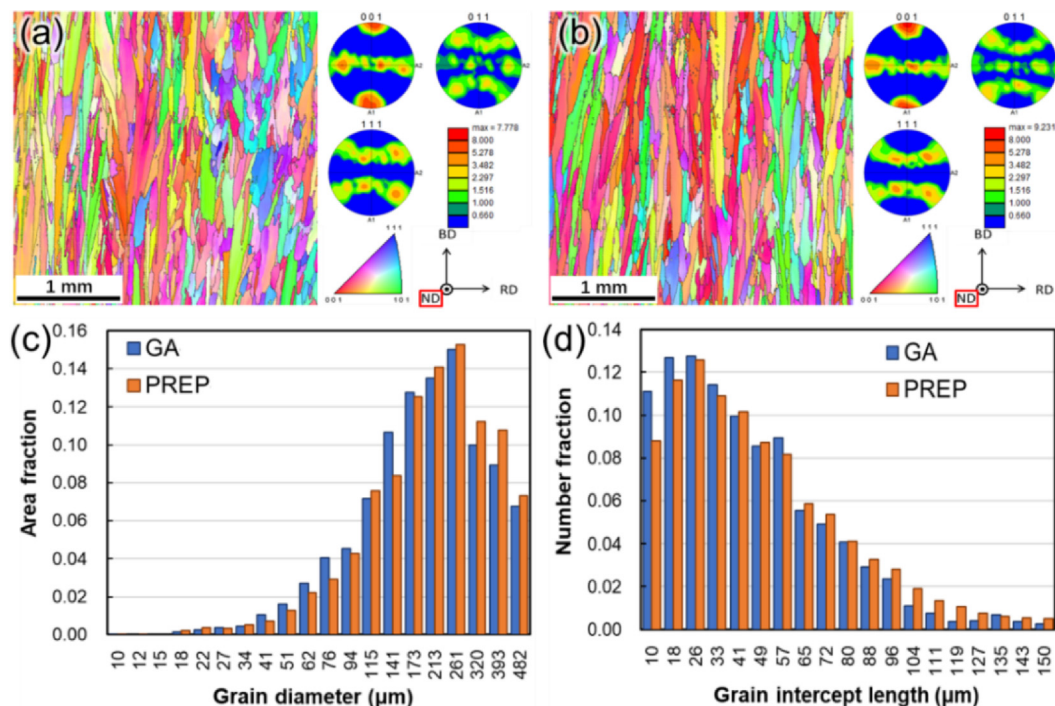
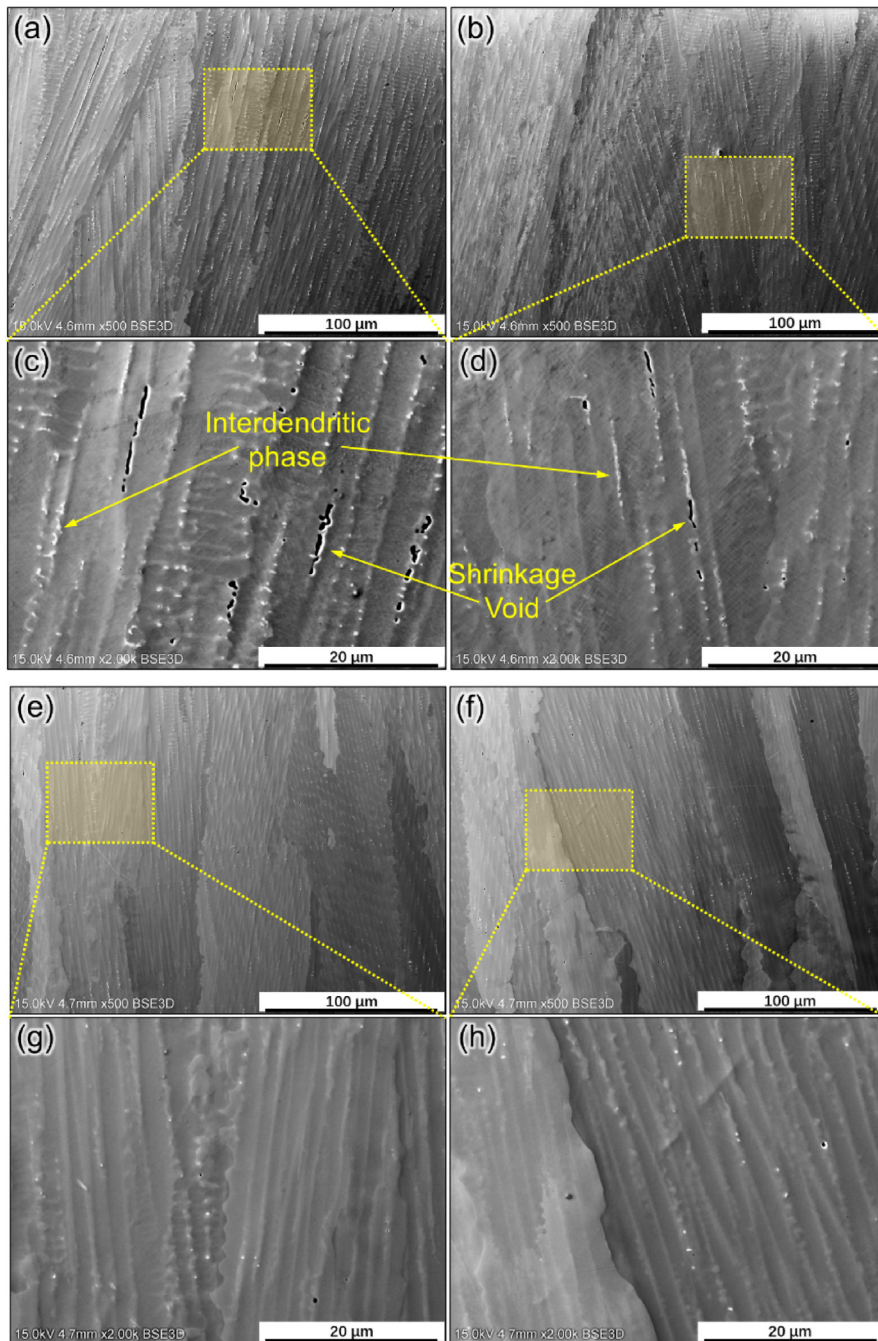


Fig. 2. EBSD inverse pole figure maps and pole figures of the samples fabricated using the (a) GA and (b) PREP powders. The sectioned view is parallel to BD. The crystallographic orientations are indicated along the normal direction (ND). The grain size is characterized by the (c) grain diameter and (d) grain intercept length.



**Fig. 3.** BSE micrographs of the grain structure at the (a)(c)(e)(g) top and (b)(d)(f)(h) middle of the (a)(b)(c)(d) GA and (e)(f)(g)(h) PREP samples.

and solidification shrinkage in the interdendritic region was rarely observed. The density that was measured through the Archimedes method showed a higher value in the PREP sample ( $8.275 \text{ g/cm}^3$ ) than that in the GA sample ( $8.067 \text{ g/cm}^3$ ). Overall, according to the observed grain structure and substructure, the utilization of the two powders did not affect grain growth; however, the differences between the GA and PREP samples were reflected in the number of the interdendritic phases and shrinkage voids.

The high-angle annular dark-field (HAADF) micrograph and diffraction patterns in Fig. 4(a) and (c), respectively, show that the interdendritic phase had a BCC structure with a lattice constant of 0.873 nm. There was no carbide present in the low-carbon CCM alloy. The STEM-EDX maps in Fig. 4(b) show that Mo, Cr, Si, Mn, and Fe were enriched in these phases. Thus, the bright precipitates

distributed in the interdendritic region were verified to be the  $\sigma$  phase, which is a brittle phase with low fracture toughness and precipitates incoherently in the interdendritic region or grain boundary [53].

Metallographic observations have local limitations. If the microstructural differences observed above were widespread throughout the two samples, there would be differences between the two samples in terms of mechanical performance. The brittle  $\sigma$  phase is not conducive for coordinated deformation between the dendrite branch and interdendritic region, and the shrinkage voids provide crack sources that trigger failure under microlocal stresses [54]. Therefore, the compression tests were performed at room temperature. The stress-strain curve in Fig. 5 shows that the PREP sample exhibits a higher strength than the GA sample.

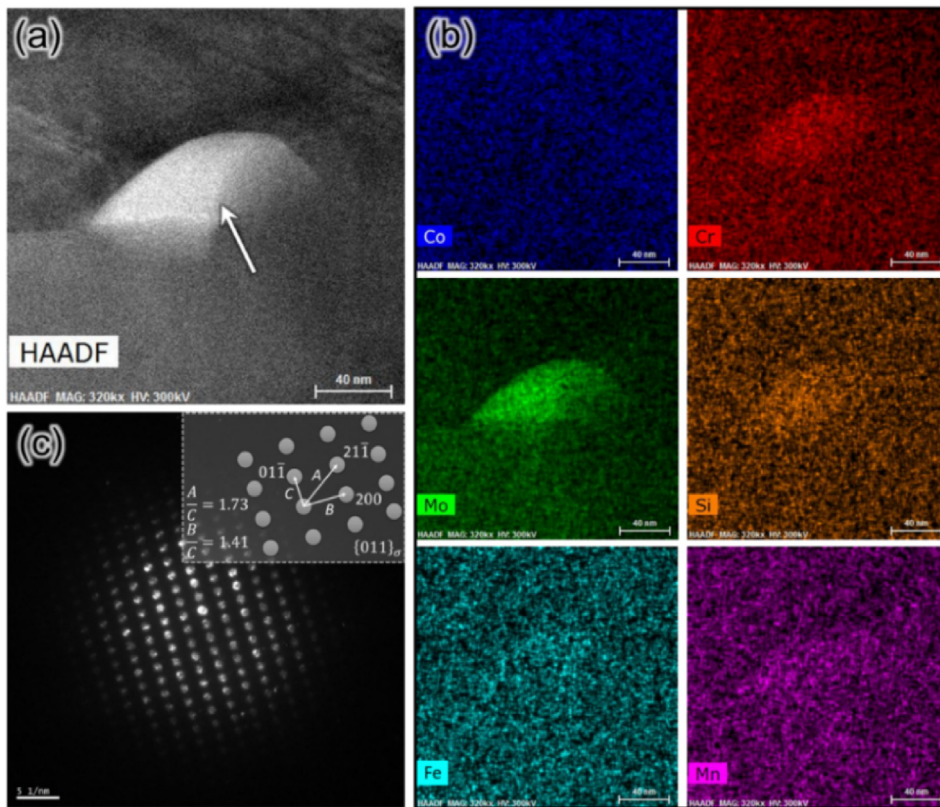


**Fig. 4.** (a) High-angle annular dark-field micrograph. (b) STEM-EDX maps show that Mo, Cr, Si, Mn, and Fe are enriched. (c) Diffraction pattern of the interdendritic phase indicates a BCC structure.

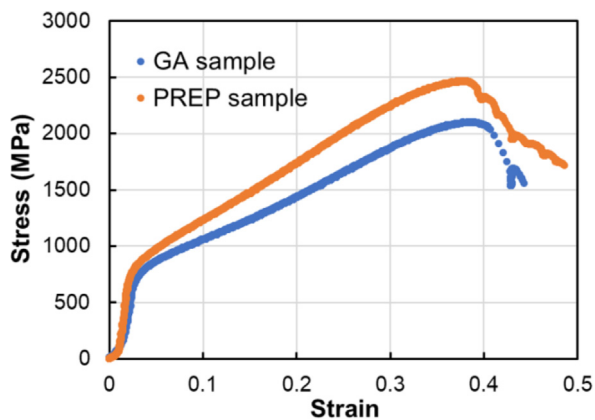


**Fig. 5.** Curves of compressive stress versus strain obtained by the compression tests.

However, the yield stress is almost equal between the two samples, and it can be observed that the difference in strength is because the PREP sample shows a significantly higher work-hardening rate than the GA sample. The difference between the PREP and GA samples in work hardening can be related to the fact that the GA sample has many voids, as shown in Fig. 3(a)–(d). Voids are the sites where dislocations are absorbed and extinguished during plastic deformation, which results in a low work-hardening rate. In contrast, the lack of voids in the PREP sample can be expected to result in a higher work-hardening behavior than the plastic deformation of the void-containing matrix. The EBSD microstructure observation results in Fig. 2 show almost no differences in the grain morphology, crystallographic texture, and

grain size of the two samples. Considering the above, the work-hardening rate of the GA sample was significantly lower than that of the PREP sample because the GA sample contained a large number of voids. Therefore, it can be inferred that the individual substructure characteristics shown in Fig. 3 are widespread throughout the GA and PREP samples. As mentioned above, the formation of the interdendritic phase and shrinkage void is related to the solidification parameters and microsegregation [55]; thus, the powder characteristics influence the non-equilibrium solidification during PBF-EB.

### 3.2. Simulation results

To accurately characterize the response of the different powders to heat transfer during PBF-EB, it is necessary to obtain powder layers with properties close to those of the actual processing [56]. Several types of preset particle clumps with elongated and satellite-like shapes were constructed by assembling default spheres in the DEM simulation. Subsequently, by adjusting the preset particle proportions with an irregular shape, the GA powder sphericity used for the DEM simulation matched the actual sphericity. In addition to assigning the corresponding PSD, the GA and PREP powders in the simulation consisted of particle clumps and perfect spheres, respectively. Moreover, because the densely solidified part is thinner than the porous powder layer, the practical thickness  $L_n$  can be expressed as  $L_n = L_0 + L_{n-1} (1 - \rho_p)$ , where  $L_0$  is the nominal thickness and  $L_{n-1}$  and  $\rho_p$  are the thickness and packing density of the previous layer, respectively. The evolution of the thickness and packing density from the first layer to the final steady layer by performing DEM simulations for each layer is shown in Supplementary Material 5. Because the GA powder had a larger overall size than the PREP powder and contained

irregular particles, the final steady (i.e., the practical) GA powder layer was thicker and had a lower packing density than the PREP powder layer.

The geometric powder layer data were inputted as the computational domain for the CtFD melting simulation. Because the fluid flow intrinsically influences the temperature field, the solidification parameters at the solidification front, including the temperature gradient ( $G$ ) and solidification rate ( $R$ ), are also affected by the molten pool behavior. In the simulations, the solidification front was represented by a cell collection whose solid fraction was greater than zero and less than one. The boundaries were considered as the isotherms of the liquidus and solidus. The  $G$  and  $R$  in this study were determined from the three cross-sections perpendicular to the scanning direction in the solidified computational domain after the molten pool with a steady state had passed. Fig. 6(a) and (b) show cut views of the CtFD-simulated molten pools via single-track melting of the GA and PREP powders. Notably, the molten pool within the PREP powder layer had a smaller volume and a more inclined S/L interface than that within the GA powder layer, which indicates that the different powder layers exhibited diverse heat transfer behaviors in response to the EB irradiation. Moreover, the solidification parameters shown in Fig. 6(c) indicate that higher  $R$  values were obtained when the PREP powder layer was melted compared to that in the case of the GA powder layer. A high  $R$  value facilitates microsegregation suppression owing to solute trapping, which is the primary reason for the lower interdendritic phase in the PREP sample. The impact of the

solidification parameters on microsegregation should be verified by PF simulation.

Fig. 7 shows the evolution of element concentrations during the Scheil solidification simulation. There was a subtle difference between the chemical compositions of the two powders. Although the curves representing the compositions of the two powders did not completely overlap, the elemental segregation trends were consistent. As solidification proceeded, the liquid phase was gradually enriched with Mo, Si, Mn, and Fe, and these elements were substantially consistent with the interdendritic  $\sigma$ -phase constituents, which indicated that the  $\sigma$ -phase formation was caused by microsegregation. Mo exhibited the most notable segregation trend during solidification as the key forming element of the  $\sigma$  phase. Therefore, non-equilibrium solidification was characterized by the spatial distribution of the Mo concentration in the PF simulation. The mean values of the solidification parameters (i.e., the  $G$ - $R$  point group centroid in Fig. 6) were applied as the 2D thermal field in the PF simulation. As an example, the solidification process obtained by performing the PF simulation with the GA powder composition and the corresponding  $G$ - $R$  values as the input is shown in Supplementary Material 6. With the dendrite growth, Mo gradually segregated into liquid between the dendrites. After solidification, chain-like Mo enrichment zones were formed with a distribution pattern similar to that of the  $\sigma$  phase in the experimental microstructure (Fig. 3).

To verify whether the compositional differences between the two powders affect solidification, PF simulations were performed

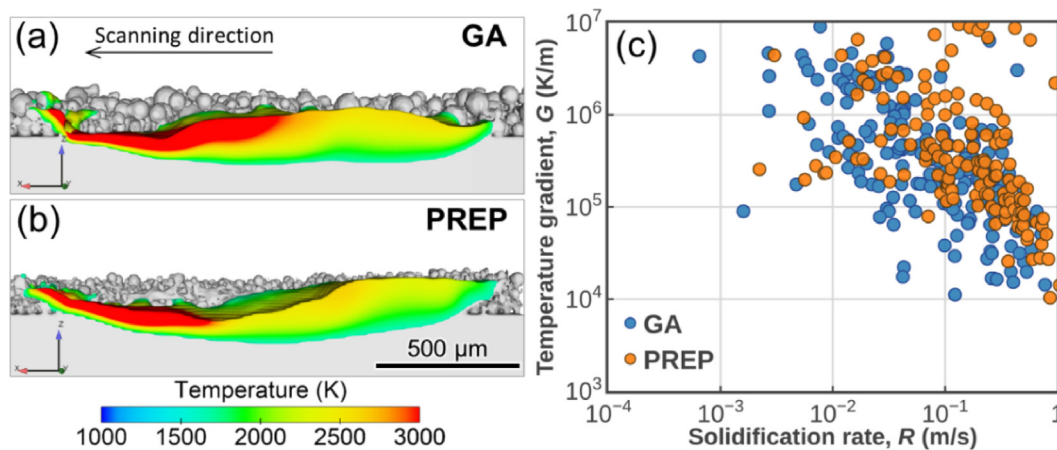


Fig. 6. CtFD-simulated molten pools formed by single-track melting on the (a) GA and (b) PREP powder layers with corresponding (c) solidification parameters.

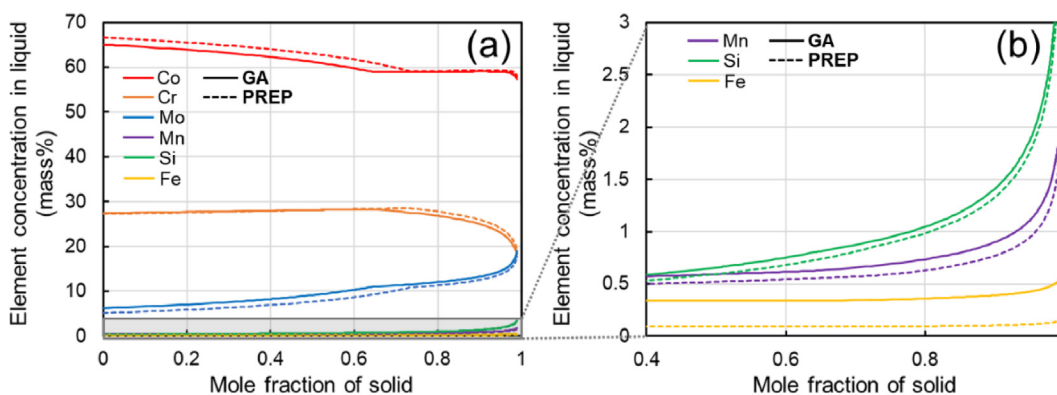
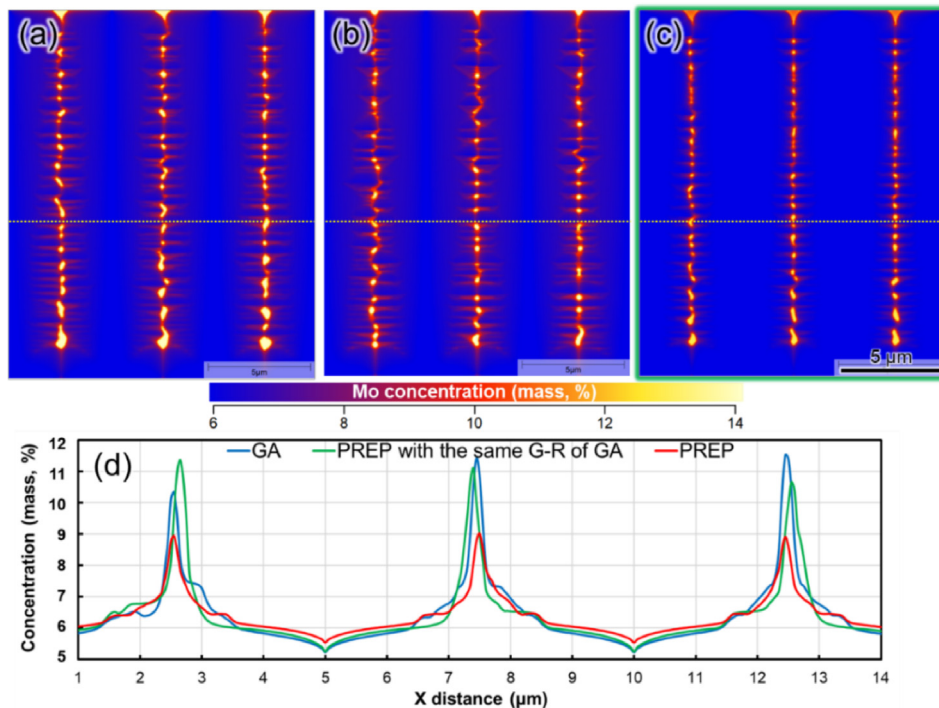


Fig. 7. Evolution of element concentrations in the liquid during the Scheil solidification simulation based on the chemical composition of the GA and PREP powders.



**Fig. 8.** PF simulations with the compositions of the (a) GA and (b) PREP powders and the mean  $G-R$  values corresponding to the GA powder as the input. (c) PF simulation with the compositions of the PREP powders and the mean  $G-R$  values corresponding to the PREP powder as the input. (d) Quantitative data of the Mo concentration at the dotted line.

with the GA (Fig. 8(a)) and PREP (Fig. 8(b)) powder compositions and the same mean  $G-R$  values corresponding to the GA powder as the input. Under a consistent thermal field, this slight compositional difference between the GA and PREP powders did not affect the solidification or degree of microsegregation. However, when the mean  $G-R$  values corresponding to the PREP powder were input with the PREP powder composition, the Mo enrichment in the interdendritic regions decreased. The results reveal that the chemical composition difference does not affect solidification. Thus, the difference in the substructure characteristics between the GA and PREP samples originated from the different heat absorption and conduction behaviors. In other words, the high  $R$  obtained by the PREP powder layer melting contributed to microsegregation suppression because of enhanced solute trapping and, subsequently, less interdendritic  $\sigma$  phases. Moreover, a comparison of Fig. 3(c) (d) and (g)(h) shows that the substructures are mainly cellular dendrites; however, because of the significant degree of microsegregation in the GA sample, the protrusion or secondary dendrite arm is more developed than that in the PREP sample. This phenomenon can hinder liquid feeding in the interdendritic region during solidification, inducing shrinkage void formation.

## 4. Discussion

### 4.1. Effect of solidification rate on micro-segregation

The experimental and simulation results confirmed that the lower number of  $\sigma$  phases and the few shrinkage voids in the interdendritic region of the PREP sample resulted from a limited degree of microsegregation during solidification. Melting on the PREP powder layer exhibited a high  $R$  to suppress microsegregation owing to the enhanced solute trapping effect. The beam scan speed directly influenced the  $R$  value of the translating molten pool [57]. For the CCM alloy system, the  $R$  value affecting microsegregation can be determined by single-track melting experiments at different

beam scan speeds. Fig. 9 shows the cross-sectional BSE micrographs of the melted region of single-track melting on the CCM alloy baseplate. With an increase in the scan speed, the number of interdendritic  $\sigma$  phases decreased. By performing the corresponding CtFD simulations, the solidification parameters shown in Fig. 10(a) and (b) illustrate that a faster beam scan causes a greater  $R$ . In the schematic (Fig. 10(c)), solute elements are ejected from solid to liquid during solidification, thereby accumulating ahead of the solidification front. Solute partitioning was determined using element diffusion kinetics. Thus, if  $R$  is higher than the solute diffusion rate, solute trapping occurs to reduce the concentration difference between the solid and liquid phases after solidification. Single-track melting experiments also verified that the microsegregation behavior of the CCM alloy system studied here could indeed be controlled by manipulating the  $R$  value.

### 4.2. Effect of powder characteristics on solidification rate

As discussed in Section 4.1,  $R$  is directly affected by the scan speed. When the scan speed (i.e., the molten pool translation speed) is fixed, the  $R$  variation depends on the molten pool geometry, which is determined by the heat transfer behavior of the surrounding solid [58,59]. The schematic in Fig. 11 shows that because the direction of  $R$  is perpendicular to the solid-liquid interface, there is a geometric relationship between  $R$  and the scan speed  $V$ :  $R = V \cos \theta$ , where  $\theta$  is the included angle between  $R$  and  $V$ . Thus, when  $V$  is a constant, a higher  $R$  corresponds to a smaller angle  $\theta$ . Notably, the molten pool geometry was affected by the heat absorption and conduction behavior when the powder layer was irradiated with the EB. On one hand, for a high heat absorptivity powder layer, the melt mass formed in a unit time is large, resulting in a molten pool with a large volume and depth. On the other hand, for a high-heat-conductivity powder layer, the latent heat generated at the solidification front can be dissipated in time, forming a molten pool with a small length. Therefore, when the

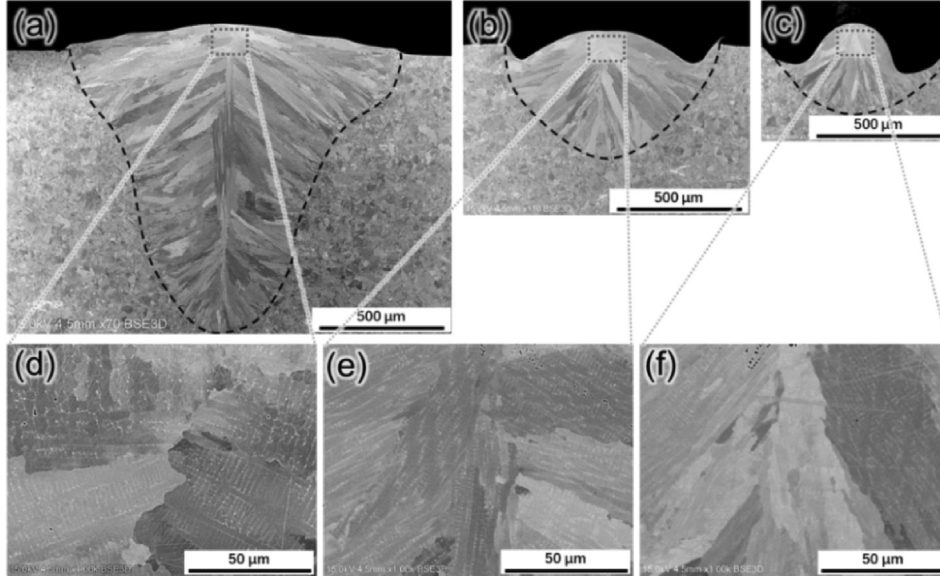


**Fig. 9.** BSE micrographs of the melted region of single-track melting on the CCM alloy baseplate with 1000 W power and at scan speeds of (a)(d) 100, (b)(e) 300, and (c)(f) 1000 mm/s.

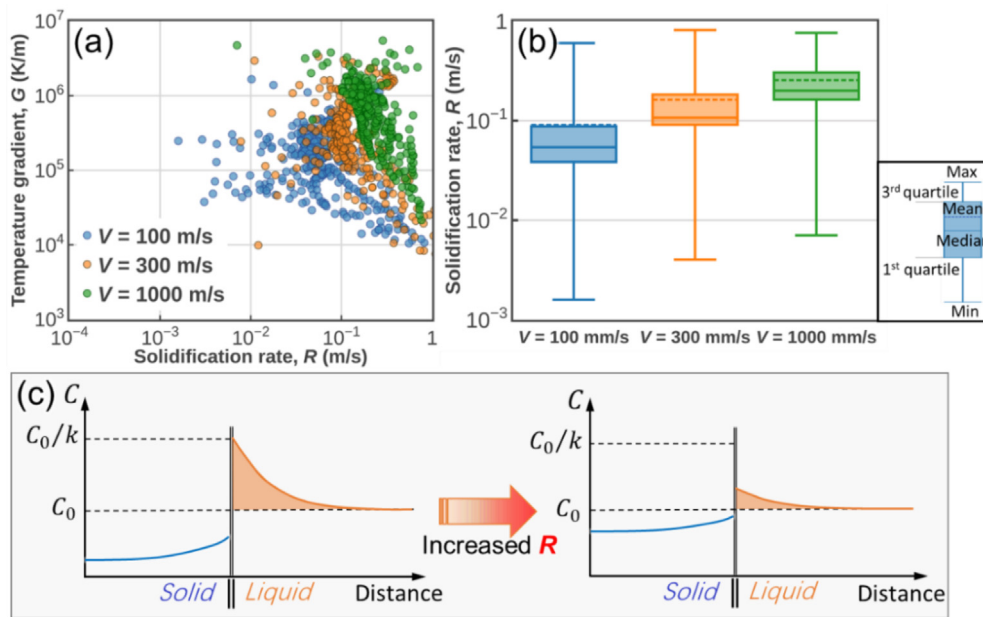


**Fig. 10.** (a) Solidification parameters obtained by performing CtFd simulations of single-track melting on the CCM alloy baseplate. (b) Box plots showing that the faster the beam scan, the higher the  $R$ . (c) Schematic showing that as solute partitioning is determined by element diffusion kinetics, a high  $R$  allows microsegregation suppression because of the enhanced solute trapping effect.

scan speed is constant,  $\theta$  is reduced for a deep and short molten pool, which increases  $R$ .

The net heat absorbed by the powder layer ( $P_{layer}$ ) depends on the difference between the EB power ( $P_{eb}$ ) and radiation heat emitted from the heated powder layer ( $P_{rad}$ ). Based on the Stefan–Boltzmann law,  $P_{layer}$  can be expressed as:

$$P_{layer} = \xi P_{eb} - \varepsilon_{layer} \sigma A (T_s^4 - T_a^4), \quad (1)$$

where  $\xi$  is the EB energy efficiency,  $\varepsilon_{layer}$  is the powder layer emissivity,  $\sigma$  is the Stefan-Boltzmann constant,  $A$  is the specific powder layer surface area, and  $T_s$  and  $T_a$  are the surface and ambient temperatures, respectively. The emissivity of the porous powder layer differs from that of a dense solid ( $\varepsilon_{solid}$ ).  $\varepsilon_{layer}$  is a function of porosity  $\phi$  and is expressed as follows: [60]

$$\varepsilon_{layer} = \frac{0.908\phi^2}{1.908\phi^2 - 2\phi + 1} \cdot \frac{\varepsilon_{solid} \left[ 2 + 3.082 \left( \frac{1-\phi}{\phi} \right)^2 \right]}{\varepsilon_{solid} \left[ 1 + 3.082 \left( \frac{1-\phi}{\phi} \right)^2 \right] + 1} + \frac{\phi^2 - 2\phi + 1}{1.908\phi^2 - 2\phi + 1} \varepsilon_{solid}. \quad (2)$$

Therefore, a powder layer with a high emissivity ( $\varepsilon_{layer}$ ) and large specific surface area ( $A$ ) exhibited a low heat absorption rate. Next, the thermal conductivity of the porous powder layer ( $\kappa_{layer}$ ) is also a function of the packing porosity  $\phi$  and is approximated as follows:

$$\kappa_{layer} = \kappa_{solid} (1 - \phi)^3, \quad (3)$$

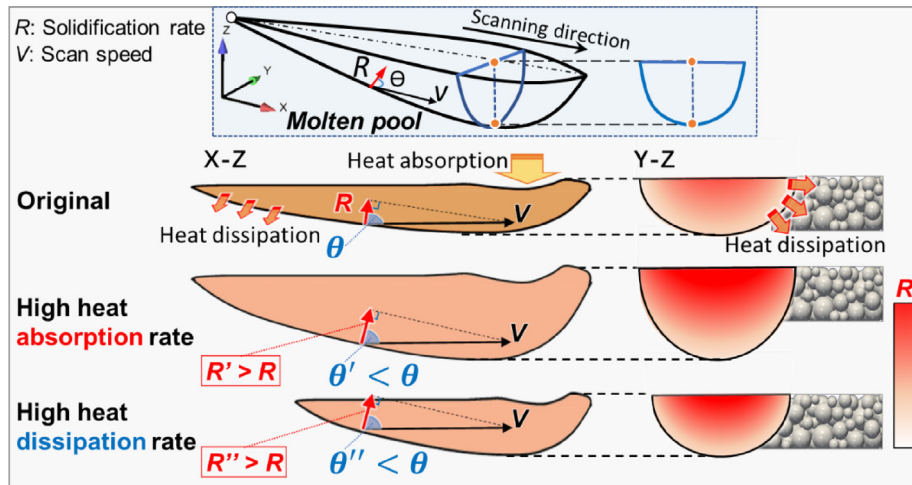


Fig. 11. Schematic showing the geometric relationship between the solidification rate  $R$  and scan speed  $V$ .

where  $\kappa_{\text{solid}}$  is the thermal conductivity of the dense solid. Therefore, a powder layer with a high packing density ( $1 - \phi$ ) exhibits a high thermal conductivity and, subsequently, a high heat dissipation rate. Notably, when the EB interacts with a material, the reflection observed when a laser is used cannot be seen; thus,  $\zeta$  is nearly unaffected by the surface profile. In summary, in the PBF-EB case, the thermal properties of the powder layer are determined by the product of the emissivity, specific surface area ( $\epsilon_{\text{layer}} \cdot A$ ), and packing density ( $1 - \phi$ ).

The GA and PREP powders studied differ in size and morphology. Fine powders have a high packing density and specific surface area [61]. The irregular powder has a large specific surface area and low packing density, unlike the perfect spherical powder, which has the highest packing density [62]. In the DEM simulation, in contrast to the irregular GA powder and spherical PREP powder, an additional powder with a PSD similar to that of the GA powder and containing perfectly spherical particles (GA-spheres) was created. Thus, the effects of the individual particle sizes and morphol-

ogy on  $R$  can be clarified. Fig. 12 shows the DEM-simulated powder layers for the three powder types. As shown by the corresponding packing density and specific surface area, although the GA powder contained irregular particles, the PREP powder had the largest specific surface area owing to its small size, which also resulted in the highest packing density. Moreover, the GA-sphere powder was the same size as the GA powder and contained only spherical particles; thus, its packing density was higher than that of the GA powder. Furthermore, the GA-sphere powder had the smallest specific surface area among the three because its mean size was larger than that of the PREP powder. Table 2 lists the calculated thermal properties of the three powder layers based on the mean values shown in Fig. 12(d). The emissivity of the porous powder layers ( $\epsilon_{\text{layer}}$ ) was higher than that of the dense solid layers ( $\epsilon_{\text{solid}}$ ); however, the difference between the three powder layers was insignificant. Because the net heat absorbed depends on  $\epsilon_{\text{layer}} \cdot A$ , the powder layer heat absorption rate increases with decreasing  $A$ . Moreover, the thermal conductivity (i.e., heat dissipation)

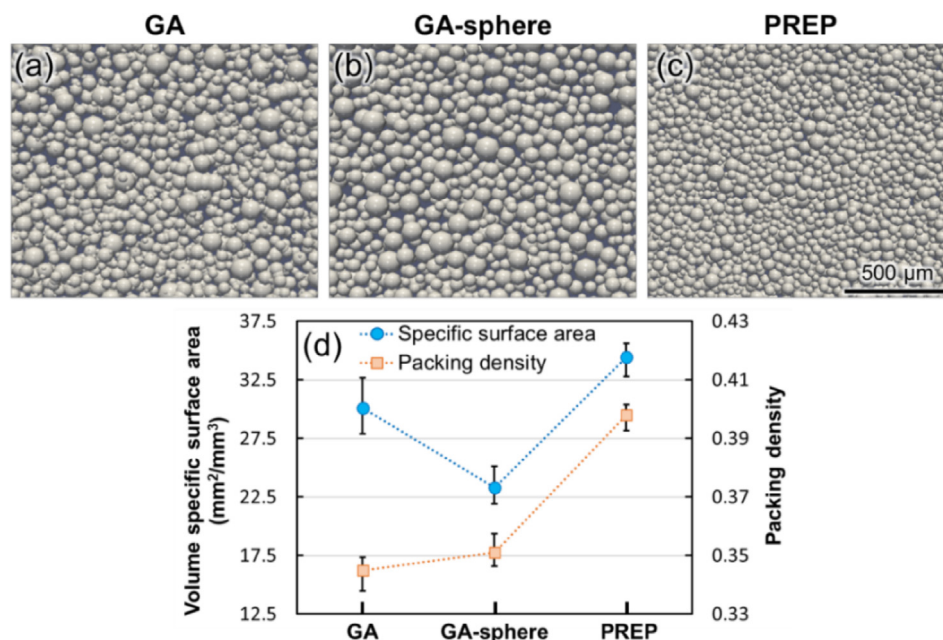


Fig. 12. DEM-simulated powder layers of the (a) GA, (b) GA-sphere, and (c) PREP powders with the (d) corresponding specific surface area and packing density. The GA-sphere powder has the same PSD as the GA powder, but the particles are perfect spheres.

**Table 2**  
Calculated variables related to the thermal properties of the three powder layers shown in Fig. 12.

	$\epsilon_{\text{solid}}$	$\kappa_{\text{solid}}$	$A$	$1 - \phi$	$\epsilon_{\text{layer}}$	$\epsilon_{\text{layer}} \cdot A$	$\kappa_{\text{layer}}$
GA	0.3	34.5	30.09	0.340	0.4912	14.78	1.36
GA-sphere			23.29	0.346	0.4918	11.45	1.43
PREP			34.45	0.393	0.4951	17.06	2.09

Unit of thermal conductivity  $\kappa$ : W/(m·K).

pation rate) of the powder layer increases with increasing  $1 - \phi$ . Therefore, although the heat absorption rate of the PREP powder layer with a small particle size was low, the highest heat dissipation rate was beneficial for increasing  $R$ . Notably, compared with the GA powder layer, the GA-sphere powder layer with spherical particles had high heat absorption and dissipation rates, which were favorable for a high  $R$ .

The spatial relationships between the solidification front normal and scanning directions are illustrated in Fig. 13 by processing the CtFD simulation results to verify the effect of the powder characteristics on  $R$ . The scanning, vertical, and horizontal directions are represented by blue, green, and red, respectively. Therefore, the spatial direction color was determined by the angle between the solidification front normal and each axis. Fig. 13(a) shows the grid collection of half of the solidification front evolving with the translating molten pool. Compared with the GA powder, the GA-sphere and PREP powders showed more grids in a color close to blue, that is, a small angle between  $R$  and  $V$ . The  $R$  box plot in Fig. 13(b) also shows that the melting of the GA-sphere and PREP powder layers generated a high  $R$ , suppressing microsegregation owing to enhanced solute trapping, and subsequently restraining the formation of the  $\sigma$  phase and shrinkage void.

In summary, on the premise of proper size control, compared with the GA powder, the PREP powder has a small specific surface area and high sphericity; thus, the generated powder layer exhibits high heat absorption and dissipation rates. Consequently, a high  $R$  is facilitated, enhancing solute trapping and suppressing microsegregation during PBF-EB-induced nonequilibrium solidification.

### 5. Conclusions

In this study, a PBF-EB-built CCM alloy was fabricated using GA and PREP powders of different particle sizes and morphologies. The mechanisms through which the powder characteristics influence the non-equilibrium solidification behavior were determined. The conclusions are as follows.

There was almost no difference in the grain morphology, grain size, or crystallographic texture between the GA and PREP samples. However, the formation of the  $\sigma$  phase and shrinkage voids in the interdendritic region was suppressed in the PREP sample, unlike that in the GA sample.

According to the simulation results, compared with the melting of the GA powder, the high  $R$  obtained by melting the PREP powder layer contributed to the suppression of microsegregation owing to the improved solute trapping.

The effect of the molten-pool morphology on  $R$  is determined by the thermal properties of the powder layer. The high-heat-absorptivity powder layer generated a molten pool with a large depth, whereas the high-heat-dissipation powder layer induced a molten pool with a small length. For a deep or short molten pool, the angle between  $R$  and the scanning direction was reduced, which increased  $R$ .

Upon appropriate size control, compared to the GA powder, the PREP powder had a small specific surface area and high sphericity; thus, the powder layer exhibited high heat absorption and dissipation rates. Consequently, a high  $R$  was facilitated, enhancing solute trapping and suppressing microsegregation during PBF-EB-induced nonequilibrium solidification.

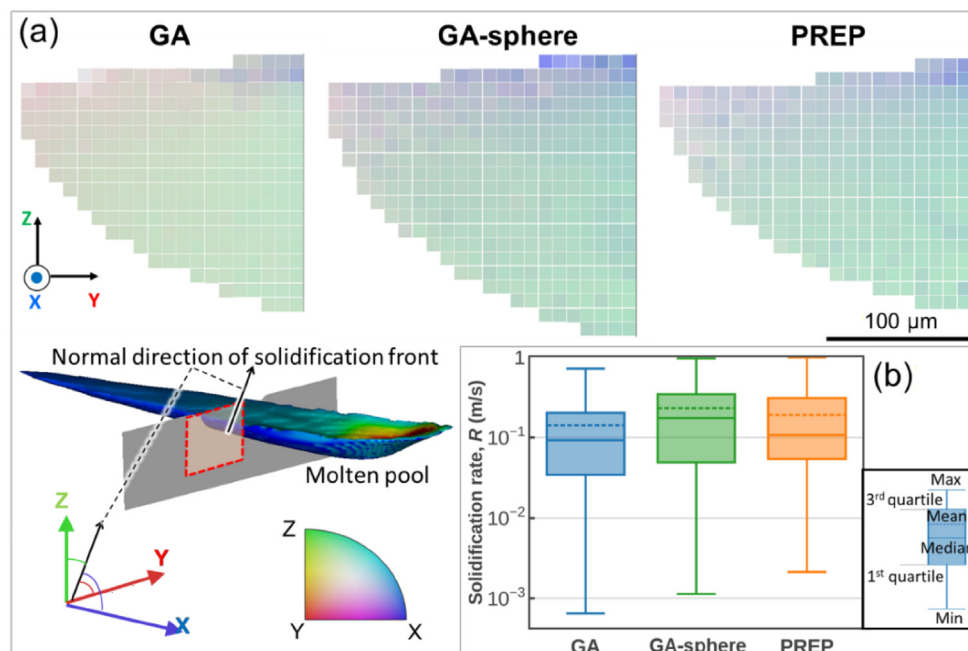


**Fig. 13.** (a) CtFD simulation results showing the spatial relationships between the normal direction of the solidification front and scanning direction. The scanning, vertical, and horizontal directions are represented by blue, green, and red, respectively. The color grid close to blue indicates a small angle between  $R$  and  $V$  and, subsequently, a high  $R$ . (b) The corresponding box plot of  $R$ .

Although the above conclusions may differ for different materials, the mechanism should be universal and provide an essential reference for selecting and optimizing metallic powders applicable to additive manufacturing. In future work, systematic comparative research on the multiple types of powders used in PBF will be conducted. Considering the premise of maintaining the spatial distribution of particles and environmental consistency during PBF, a feasible experimental method for measuring the thermal physical properties of the powder layer will be implemented, and a feedback iteration will be formed with the numerical simulation to obtain more universal, accurate, and quantitative research conclusions.

#### CRediT authorship contribution statement

**Yufan Zhao:** Writing – original draft, Conceptualization, Methodology, Formal analysis, Visualization. **Huakang Bian:** Investigation, Writing – review & editing, Supervision. **Hao Wang:** Investigation, Resources. **Aoyagi Kenta:** Resources, Methodology. **Yamanaka Kenta:** Supervision. **Akihiko Chiba:** Writing – review & editing, Supervision, Project administration, Funding acquisition.

#### Data availability

The raw/processed data required to reproduce these findings cannot be shared at this time as the data also forms part of an ongoing study.

#### Declaration of Competing Interest

The authors declare that they have no known competing financial interests or personal relationships that could have appeared to influence the work reported in this paper.

#### Acknowledgments

This work was supported by JSPS KAKENHI [grant number 18H03834, 21k14432]; the Cross-Ministerial Strategic Innovation Promotion Program (SIP) of Japan Science and Technology (JST); the Japan Ministry of Economy, Trade and Industry (METI); the New Energy and Industrial Technology Development Organization (NEDO); the Technology Research Association for Future Additive Manufacturing (TRAFAM); and the “Creation of Life Innovation Materials for Interdisciplinary and International Researcher Development” project. This work was also supported by the “Fundamental Research Funds for the Central Universities” [grant number G2021KY05104]. We would like to thank Editage (www.editage.com) for English language editing.

#### Appendix A. Supplementary material

Supplementary data to this article can be found online at <https://doi.org/10.1016/j.matdes.2022.110915>.

#### References

- [1] Y. Kok, X.P. Tan, P. Wang, M.L.S. Nai, N.H. Loh, E. Liu, S.B. Tor, Anisotropy and heterogeneity of microstructure and mechanical properties in metal additive manufacturing: a critical review, *Mater. Des.* 139 (2018) 565–586, <https://doi.org/10.1016/j.matdes.2017.11.021>.
- [2] T. DebRoy, H.L. Wei, J.S. Zuback, T. Mukherjee, J.W. Elmer, J.O. Milewski, A.M. Beese, A. Wilson-Heid, A. De, W. Zhang, Additive manufacturing of metallic components – Process, structure and properties, *Prog. Mater. Sci.* 92 (2018) 112–224, <https://doi.org/10.1016/j.pmatsci.2017.10.001>.
- [3] R. Seede, J. Ye, A. Whitt, W. Trehern, A. Elwany, R. Arroyave, I. Karaman, Effect of composition and phase diagram features on printability and microstructure in laser powder bed fusion: Development and comparison of processing maps

- across alloy systems, *Addit. Manuf.* 47 (2021), <https://doi.org/10.1016/j.addma.2021.102258> 102258.
- [4] Y. Zhou, Y.-S. Che, C. Wang, R. Liu, S.-F. Wen, Selective laser melting high-performance ZrC-reinforced tungsten composites with tailored microstructure and suppressed cracking susceptibility, *Tungsten*. 3 (2021) 72–88, <https://doi.org/10.1007/s42864-021-00076-8>.
- [5] R. Shi, S.A. Khairallah, T.T. Roehling, T.W. Heo, J.T. McKeown, M.J. Matthews, Microstructural control in metal laser powder bed fusion additive manufacturing using laser beam shaping strategy, *Acta Mater.* 184 (2020) 284–305, <https://doi.org/10.1016/j.actamat.2019.11.053>.
- [6] W.W. Shao, B. Zhang, Y. Liu, C.S. Liu, P. Tan, S. Shang, G.P. Zhang, Effect of laser power on porosity and mechanical properties of GH4169 fabricated by laser melting deposition, *Tungsten*. 1 (2019) 297–305, <https://doi.org/10.1007/s42864-020-00034-w>.
- [7] C.J. Todaro, M.A. Easton, D. Qiu, D. Zhang, M.J. Birmingham, E.W. Lui, M. Brandt, D.H. StJohn, M. Qian, Grain structure control during metal 3D printing by high-intensity ultrasound, *Nat. Commun.* 11 (2020) 1–9, <https://doi.org/10.1038/s41467-019-13874-z>.
- [8] C.L.A. Leung, R. Tosi, E. Muzangaza, S. Nonni, P.J. Withers, P.D. Lee, Effect of preheating on the thermal, microstructural and mechanical properties of selective electron beam melted Ti-6Al-4V components, *Mater. Des.* 174 (2019), <https://doi.org/10.1016/j.matdes.2019.107792> 107792.
- [9] R. Seede, B. Zhang, A. Whitt, S. Picak, S. Gibbons, P. Flater, A. Elwany, R. Arroyave, I. Karaman, Effect of heat treatments on the microstructure and mechanical properties of an ultra-high strength martensitic steel fabricated via laser powder bed fusion additive manufacturing, *Addit. Manuf.* 47 (2021), <https://doi.org/10.1016/j.addma.2021.102255> 102255.
- [10] R. Schur, S. Ghods, C. Wisdom, R. Pahuja, A. Montelione, D. Arola, M. Ramulu, Mechanical anisotropy and its evolution with powder reuse in Electron Beam Melting AM of Ti6Al4V, *Mater. Des.* 200 (2021), <https://doi.org/10.1016/j.matdes.2021.109450> 109450.
- [11] C. Zhong, J. Chen, S. Linnenbrink, A. Gasser, S. Sui, R. Poprawe, A comparative study of Inconel 718 formed by High Deposition Rate Laser Metal Deposition with GA powder and PREP powder, *Mater. Des.* 107 (2016) 386–392, <https://doi.org/10.1016/j.matdes.2016.06.037>.
- [12] X. Lin, Y.Q. Cao, Z.T. Wang, J. Cao, L.L. Wang, W.D. Huang, Regular eutectic and anomalous eutectic growth behavior in laser remelting of Ni-30wt%Sn alloys, *Acta Mater.* 126 (2017) 210–220, <https://doi.org/10.1016/j.actamat.2016.12.061>.
- [13] X. Yang, W.-J. Ma, Y.-J. Ren, S.-F. Liu, Y. Wang, W.-L. Wang, H.-P. Tang, Subgrain microstructures and tensile properties of 316L stainless steel manufactured by selective laser melting, *J. Iron. Steel Res. Int.* 28 (9) (2021) 1159–1167.
- [14] S. Chandra, X. Tan, R.L. Narayan, C. Wang, S.B. Tor, G. Seet, A generalised hot cracking criterion for nickel-based superalloys additively manufactured by electron beam melting, *Addit. Manuf.* 37 (2021), <https://doi.org/10.1016/j.addma.2020.101633> 101633.
- [15] T. Keller, G. Lindwall, S. Ghosh, L. Ma, B.M. Lane, F. Zhang, U.R. Kattner, E.A. Lass, J.C. Heigel, Y. Idell, M.E. Williams, A.J. Allen, J.E. Guyer, L.E. Levine, Application of finite element, phase-field, and CALPHAD-based methods to additive manufacturing of Ni-based superalloys, *Acta Mater.* 139 (2017) 244–253, <https://doi.org/10.1016/j.actamat.2017.05.003>.
- [16] J. Xu, X. Lin, Y. Zhao, P. Guo, X. Wen, Q. Li, H. Yang, H. Dong, L. Xue, W. Huang, HAZ Liquid Cracking Mechanism of IN-738LC Superalloy Prepared by Laser Solid Forming, *Metall. Mater. Trans. A: Phys. Metall. Mater. Sci.* 49 (2018) 5118–5136, <https://doi.org/10.1007/s11661-018-4826-6>.
- [17] H. Liu, Z.-z. Huang, D.-J. Yu, D.-L. Hu, H.-G. Zhong, Q.-J. Zhai, J.-X. Fu, Effect of cooling rate on microstructure and inclusion in non-quenched and tempered steel during horizontal directional solidification, *J. Iron. Steel Res. Int.* 26 (9) (2019) 973–982.
- [18] V. Bathula, C. Liu, K. Zwiackier, J. McKeown, J.M.K. Wiezorek, Interface velocity dependent solute trapping and phase selection during rapid solidification of laser melted hypo-eutectic Al-11at.%Cu alloy, *Acta Materialia*. 195 (2020) 341–357, <https://doi.org/10.1016/j.actamat.2020.04.006>.
- [19] P. Nie, O.A. Ojo, Z. Li, Numerical modeling of microstructure evolution during laser additive manufacturing of a nickel-based superalloy, *Acta Mater.* 77 (2014) 85–95, <https://doi.org/10.1016/j.actamat.2014.05.039>.
- [20] C. Kumara, A.R. Balachandramurthi, S. Goel, F. Hanning, J. Moverare, Toward a better understanding of phase transformations in additive manufacturing of Alloy 718, *Materialia*. 13 (2020), <https://doi.org/10.1016/j.mta.2020.100862> 100862.
- [21] X. Wang, P.W. Liu, Y. Ji, Y. Liu, M.H. Horstemeyer, L. Chen, Investigation on Microsegregation of IN718 Alloy During Additive Manufacturing via Integrated Phase-Field and Finite-Element Modeling, *J. Mater. Eng. Perform.* 28 (2019) 657–665, <https://doi.org/10.1007/s11665-018-3620-3>.
- [22] H. Xiao, S. Li, X. Han, J. Mazumder, L. Song, Laves phase control of Inconel 718 alloy using quasi-continuous-wave laser additive manufacturing, *Mater. Des.* 122 (2017) 330–339, <https://doi.org/10.1016/j.matdes.2017.03.004>.
- [23] Y. Wang, J. Shi, Influence of laser scan speed on micro-segregation in selective laser melting of an iron-carbon alloy: A multi-scale simulation study, *Procedia Manufacturing*, Elsevier B.V. (2018) 941–951, <https://doi.org/10.1016/j.promfg.2018.07.121>.
- [24] Y. Chen, F. Lu, K. Zhang, P. Nie, S.R. Elmi Hosseini, K. Feng, Z. Li, Dendritic microstructure and hot cracking of laser additive manufactured Inconel 718 under improved base cooling, *J. Alloy. Compd.* 670 (2016) 312–321, <https://doi.org/10.1016/j.jallcom.2016.01.250>.

- [25] Y.C. Zhang, Z.G. Li, P.L. Nie, Y.X. Wu, Effect of ultrarapid cooling on microstructure of laser cladding IN718 coating, *Surf. Eng.* 29 (2013) 414–418, <https://doi.org/10.1179/1743294413Y.0000000142>.
- [26] Y. Zhao, Y. Koizumi, K. Aoyagi, K. Yamanaka, A. Chiba, Thermal properties of powder beds in energy absorption and heat transfer during additive manufacturing with electron beam, *Powder Technol.* 381 (2021) 44–54, <https://doi.org/10.1016/j.powtec.2020.11.082>.
- [27] Y. Zhao, K. Aoyagi, Y. Daino, K. Yamanaka, A. Chiba, Significance of powder feedstock characteristics in defect suppression of additively manufactured Inconel 718, *Addit. Manuf.* 34 (2020), <https://doi.org/10.1016/j.addma.2020.101277> 101277.
- [28] J.H. Tan, W.L.E. Wong, K.W. Dalgarno, An overview of powder granulometry on feedstock and part performance in the selective laser melting process, *Addit. Manuf.* 18 (2017) 228–255, <https://doi.org/10.1016/j.addma.2017.10.011>.
- [29] Y. Koizumi, A. Okazaki, A. Chiba, T. Kato, A. Takezawa, Cellular lattices of biomedical Co–Cr–Mo alloy fabricated by electron beam melting with the aid of shape optimization, *Addit. Manuf.* 12 (2016) 305–313, <https://doi.org/10.1016/j.addma.2016.06.001>.
- [30] M. Galati, L. Iuliano, A literature review of powder-based electron beam melting focusing on numerical simulations, *Addit. Manuf.* 19 (2018) 1–20, <https://doi.org/10.1016/j.addma.2017.11.001>.
- [31] C. Kumara, D. Deng, F. Hanning, M. Raanes, J. Moverare, P. Nylén, Predicting the Microstructural Evolution of Electron Beam Melting of Alloy 718 with Phase-Field Modeling, *Metallurgical and Materials Transactions A: Physical Metallurgy and Materials*, Science 50 (2019) 2527–2537, <https://doi.org/10.1007/s11661-019-05163-7>.
- [32] S. Özbilen, Satellite formation mechanism in gas atomized powders, *Powder Metall.* 42 (1999) 70–78, <https://doi.org/10.1179/pom.1999.42.1.70>.
- [33] M. Wei, S. Chen, M. Sun, J. Liang, C. Liu, M. Wang, Atomization simulation and preparation of 24CrNiMoY alloy steel powder using VIGA technology at high gas pressure, *Powder Technol.* 367 (2020) 724–739, <https://doi.org/10.1016/j.powtec.2020.04.030>.
- [34] Y. Zhao, Y. Cui, H. Numata, H. Bian, K. Wako, K. Yamanaka, K. Aoyagi, A. Chiba, Centrifugal granulation behavior in metallic powder fabrication by plasma rotating electrode process, *Sci. Rep.* 10 (2020) 18446, <https://doi.org/10.1038/s41598-020-75503-w>.
- [35] J.O. Andersson, T. Helander, L. Höglund, P. Shi, B. Sundman, Thermo-Calc & DICTRA, computational tools for materials science, CALPHAD: Comput. Coupling Phase Diagrams Thermochem. 26 (2002) 273–312, [https://doi.org/10.1016/S0364-5916\(02\)00037-8](https://doi.org/10.1016/S0364-5916(02)00037-8).
- [36] D. Gu, M. Xia, D. Dai, On the role of powder flow behavior in fluid thermodynamics and laser processability of Ni-based composites by selective laser melting, *Int. J. Mach. Tools Manuf.* 137 (2019) 67–78, <https://doi.org/10.1016/j.ijmactools.2018.10.006>.
- [37] Y. Zeng, F. Jia, Y. Zhang, X. Meng, Y. Han, H. Wang, DEM study to determine the relationship between particle velocity fluctuations and contact force disappearance, *Powder Technol.* 313 (2017) 112–121, <https://doi.org/10.1016/j.powtec.2017.03.022>.
- [38] Václav Šmilauer, Emanuele Catalano, Bruno Chareyre, Sergei Dorofeenko, Jerome Duriez, Nolan Dyck, Jan Elias, Burak Er, Alexander Eulitz, Anton Gladky, Ning Guo, Christian Jakob, Francois Kneib, Janek Kozicki, Donia Marzougui, Raphael Maurin, Chiara Modenese, Luc Scholtes, Luc Sibille, Janek Stransky, Thomas Sweijen, Klaus Thoeni, Chao Yuan, Yade Documentation 2nd ed. The Yade Project., (2015). <https://doi.org/10.5281/zenodo.34073>.
- [39] J. Wang, D. Yao, M. Li, X. An, S. Li, W. Hou, X. Zhang, G. Yang, J. Wang, L. Wang, Hierarchical effects of multi-layer powder spreading in the electron beam powder bed fusion additive manufacturing of pure tungsten material, *Addit. Manuf.* 55 (2022), <https://doi.org/10.1016/j.addma.2022.102835> 102835.
- [40] D. Dai, D. Gu, Q. Ge, C. Ma, X. Shi, H. Zhang, Thermodynamics of molten pool predicted by computational fluid dynamics in selective laser melting of Ti6Al4V: Surface morphology evolution and densification behavior, *CMES - Computer Modeling in Engineering and Sciences*. 124 (2020) 1085–1098. <https://doi.org/10.32604/cmescs.2020.010927>.
- [41] Inc. FlowScience, FLOW-3D<sup>®</sup> Version 11.2 [Computer software], (2017). <https://www.flow3d.com>.
- [42] Y. Zhao, Y. Koizumi, K. Aoyagi, D. Wei, K. Yamanaka, A. Chiba, Molten pool behavior and effect of fluid flow on solidification conditions in selective electron beam melting (SEBM) of a biomedical Co–Cr–Mo alloy, *Addit. Manuf.* 26 (2019) 202–214, <https://doi.org/10.1016/j.addma.2018.12.002>.
- [43] Y. Zhao, K. Aoyagi, K. Yamanaka, A. Chiba, Role of operating and environmental conditions in determining molten pool dynamics during electron beam melting and selective laser melting, *Addit. Manuf.* 36 (2020), <https://doi.org/10.1016/j.addma.2020.101559> 101559.
- [44] J.T. McKeown, A.J. Clarke, J.M.K. Wiezorek, Imaging transient solidification behavior, *MRS Bull.* 45 (2020) 916–926, <https://doi.org/10.1557/mrs.2020.273>.
- [45] MICRESS<sup>®</sup> - The MICROstructure Evolution Simulation Software, (n.d.).
- [46] I. Steinbach, F. Pezzolla, B. Nestler, M. Seeßelberg, R. Prieler, G.J. Schmitz, J.L.L. Rezende, A phase field concept for multiphase systems, *Physica D* 94 (1996) 135–147, [https://doi.org/10.1016/0167-2789\(95\)00298-7](https://doi.org/10.1016/0167-2789(95)00298-7).
- [47] C. Guo, J. Li, H. Yu, Z. Wang, X. Lin, J. Wang, Branching-induced grain boundary evolution during directional solidification of columnar dendritic grains, *Acta Mater.* 136 (2017) 148–163, <https://doi.org/10.1016/j.actamat.2017.07.002>.
- [48] C. Kumara, A. Segerstark, F. Hanning, N. Dixit, S. Joshi, J. Moverare, P. Nylén, Microstructure modelling of laser metal powder directed energy deposition of alloy 718, *Addit. Manuf.* 25 (2019) 357–364, <https://doi.org/10.1016/j.addma.2018.11.024>.
- [49] Y. Zhao, Y. Koizumi, K. Aoyagi, D. Wei, K. Yamanaka, A. Chiba, Comprehensive study on mechanisms for grain morphology evolution and texture development in powder bed fusion with electron beam of Co–Cr–Mo alloy, *Materialia*. 6 (2019), <https://doi.org/10.1016/j.mtla.2019.100346>.
- [50] S. Paul, J. Liu, S.T. Strayer, Y. Zhao, S. Sridar, M.A. Klecka, W. Xiong, A.C. To, A Discrete Dendrite Dynamics Model for Epitaxial Columnar Grain Growth in Metal Additive Manufacturing with Application to Inconel, *Addit. Manuf.* 36 (2020), <https://doi.org/10.1016/j.addma.2020.101611> 101611.
- [51] X.P. Tan, S. Chandra, Y. Kok, S.B. Tor, G. Seet, N.H. Loh, E. Liu, Revealing competitive columnar grain growth behavior and periodic microstructural banding in additively manufactured Ti-6Al-4 V parts by selective electron beam melting, *Materialia*. 7 (2019), <https://doi.org/10.1016/j.mtla.2019.100365> 100365.
- [52] D.R. Alkeland, P.P. Phule, *Essentials of Materials Science and Engineering*, Cengage Learning, 2004.
- [53] Y. Chen, Y. Li, S. Kurosu, K. Yamanaka, N. Tang, Y. Koizumi, A. Chiba, Effects of sigma phase and carbide on the wear behavior of CoCrMo alloys in Hanks' solution, *Wear* 310 (2014) 51–62, <https://doi.org/10.1016/j.wear.2013.12.010>.
- [54] M. Galati, A. Snis, L. Iuliano, Powder bed properties modelling and 3D thermo-mechanical simulation of the additive manufacturing Electron Beam Melting process, *Addit. Manuf.* 30 (2019), <https://doi.org/10.1016/j.addma.2019.100897> 100897.
- [55] S. Chandra, X. Tan, R.L. Narayan, M. Descoins, D. Mangelinck, S.B. Tor, E. Liu, G. Seet, Nanometer-scale precipitations in a selective electron beam melted nickel-based superalloy, *Scr. Mater.* 194 (2021), <https://doi.org/10.1016/j.scriptamat.2020.113661> 113661.
- [56] M. Galati, L. Iuliano, A. Salmi, E. Atzeni, Modelling energy source and powder properties for the development of a thermal FE model of the EBM additive manufacturing process, *Addit. Manuf.* 14 (2017) 49–59, <https://doi.org/10.1016/j.addma.2017.01.001>.
- [57] P. Mohammadpour, A. Plotkowski, A.B. Phillion, Revisiting solidification microstructure selection maps in the frame of additive manufacturing, *Addit. Manuf.* 31 (2020), <https://doi.org/10.1016/j.addma.2019.100936> 100936.
- [58] K. Zweacker, J.T. McKeown, C. Liu, T. Lagrange, B.W. Reed, G.H. Campbell, J.M. K. Wiezorek, Determination of crystal growth rates during rapid solidification of polycrystalline aluminum by nano-scale spatio-temporal resolution in situ transmission electron microscopy, *J. Appl. Phys.* 120 (2016) 55106, <https://doi.org/10.1063/1.4960443>.
- [59] J. Liu, A.C. To, Quantitative texture prediction of epitaxial columnar grains in additive manufacturing using selective laser melting, *Addit. Manuf.* 16 (2017) 58–64, <https://doi.org/10.1016/j.addma.2017.05.005>.
- [60] S. Sumin Sih, J.W. Barlow, The prediction of the emissivity and thermal conductivity of powder beds, *Part. Sci. Technol.* 22 (2004) 291–304, <https://doi.org/10.1080/02726350490501682a>.
- [61] A. Averdick, C. Cola, S.E. Zeltmann, N. Gupta, Effect of particle size distribution on the packing of powder beds: A critical discussion relevant to additive manufacturing, *Mater. Today Commun.* 24 (2020), <https://doi.org/10.1016/j.mtcomm.2020.100964> 100964.
- [62] Q.B. Nguyen, M.L.S. Nai, Z. Zhu, C.N. Sun, J. Wei, W. Zhou, Characteristics of Inconel Powders for Powder-Bed Additive Manufacturing, *Engineering*. 3 (2017) 695–700, <https://doi.org/10.1016/j.ENG.2017.05.012>.